Li et al. *Zool. Res.* 2025, 46(3): 684−694
https://doi.org/10.24272/j.issn.2095-8137.2024.360
https://cstr.cn/32248.14.zr.2024.360

ZR | Zoological Research

Article Open Access

Zic3 represses anterior digit development in tetrapods

Shan-Shan Li[1,#], Shi-Bin Bai[1,#], Xiao-Fei Sun[2], Cheng-Hua Yu[2], Yi-Ning Tang[1], Zi-Qiu Jia[1], Xiao-Ping Li[1], Song-Yang Shang[1], David M. Irwin[3], Jun Li[2,*], Zhe Wang[1,*]

[1] *College of Animal Science and Veterinary Medicine*, *Shenyang Agricultural University*, *Shenyang*, *Liaoning* 110866, *China*
[2] *Department of Obstetrics and Gynecology*, *Shengjing Hospital of China Medical University*, *Shenyang*, *Liaoning* 110004, *China*
[3] *Department of Laboratory Medicine and Pathobiology*, *University of Toronto*, *Toronto*, *Ontario M5S 1A8*, *Canada*

ABSTRACT

Pentadactyl limbs represent a conserved morphological feature among tetrapods, with anterior digits considered more important than posterior digits for refined movement. While posterior digit formation is governed by graded expression of the *Shh* and 5'*Hox* genes, the regulatory mechanisms underlying anterior digit development, especially digit I (DI), remain poorly defined. This study identified an anterior expression pattern of *Zic3* in the limb buds of representative tetrapods, including humans, which exerted an inhibitory effect on skeletal development. *Zic3* was highly expressed in the anterior region of limb buds at early developmental stages, with species-specific divergence emerging during later development. Overexpression of *Zic3* significantly delayed chondrogenesis and ossification, leading to bone shortening but not loss. Furthermore, RNA sequencing demonstrated that *Zic3* down-regulated key genes associated with skeletal development, including *Cytl1*, *Sox9, Ihh*, *Ptch1*, *Runx2*, and *Wnt16*. These findings demonstrate that *Zic3* acts as a conserved inhibitor of anterior skeletal maturation and contributes to the molecular asymmetry of tetrapod limb development.

Keywords: Tetrapod; *Zic3*; Limb development; Anterior digits; Transcriptome

INTRODUCTION

Since the emergence of tetrapods, their autopod structure has undergone extensive diversification, largely driven by modifications in the expression of anterior-posterior (AP) axis genes during embryonic development (Zhang et al., 2024). Anterior limb bud identity is established by the expression of a limited set of genes, including *Zic3*, *Gli3*, *Alx4*, and *Pax9*, while the posterior domain is defined by a broader array of well-characterized markers, such as *Shh*, *Hand2*, *Ptch1*, and 5'*Hox* (Cao et al., 2019; Stewart et al., 2019; Zhang et al., 2024). Digit-specific morphological variation is thought to originate from the antagonistic action of *Gli3* on the anterior side and the gradient of expression of the 5'*Hox* genes induced by *Shh* (Bastida et al., 2020; Litingtung et al., 2002; Wang et al., 2000). Digit I (DI), exemplified by the human thumb, represents the most anterior digit and exhibits distinct structural features, including a biphalangeal arrangement and shortened metacarpal or metatarsal elements. It plays a crucial role in facilitating precise limb movements such as digging, grasping, capturing, and climbing (Oberg, 2014; Saxena et al., 2017). Loss of *Shh* signaling can result in the formation of a single digit (Zhu et al., 2022), while targeted knockout of *Gli3*, *Alx4*, or *Pax9* produces preaxial polydactyly or duplication of DI in murine models (Panman et al., 2005; Phillips et al., 2019; Quinn et al., 2012). Notably, loss of *Zic3* function suppresses ectopic *Shh* expression in mouse forelimb buds generated by *Gli3* (+/−), thereby restoring a normal digit pattern and rescuing DI duplication (Quinn et al., 2012). These findings indicate the existence of a distinct regulatory mechanism governing DI formation and suggest *Zic3* as a potential modulator of anterior digit identity. However, the molecular basis underlying the specification and morphological patterning of anterior digits, including DI, remains poorly understood (Chiang et al., 2001; McQueen & Towers, 2020).

Nucleotide substitutions in *Zic3* have been implicated in VATER/VACTERL syndrome (Hilger et al., 2015; Thiem et al., 2022), a rare disease characterized by the non-random co-occurrence of vertebral defects (V), anorectal malformations (A), cardiac defects (C), tracheoesophageal fistula with or without esophageal atresia (TE), renal malformations (R), and limb defects (L) (MIM# 192350). Mice carrying *Zic3* mutations exhibit a variety of developmental anomalies, including defects in cardiac morphogenesis, axial skeletal patterning, and neural tube closure (Inoue et al., 2007; Purandare et al., 2002). In some cases, certain gene mutations or complete gene knockout produce more severe phenotypes or trigger compensatory responses that obscure the functional role of

Received: 23 December 2024; Accepted: 17 February 2025; Online: 18 February 2025

Foundation items: This work was supported by the Department of Science & Technology of Liaoning Province (2024-MS-099, 2024-BS-093)

[#]Authors contributed equally to this work

*Corresponding authors, E-mail: 15640216688@163.com; zwang@syau.edu.cn

Zic3 (Sutherland et al., 2013).

To investigate its role in limb development, *Zic3* expression was examined in the limb buds of diverse tetrapod species. In all taxa analyzed, *Zic3* was highly expressed in the anterior region of the limb buds. Overexpression of human, mouse, or chicken *Zic3* in chick embryo limbs consistently produced a shortened limb phenotype, accompanied by transcriptional repression of multiple genes and pathways involved in skeletal development. Down-regulated genes were associated with extracellular matrix (ECM)-receptor interactions and focal adhesion (FA), as well as the hedgehog (HH), calcium signaling, and mitogen-activated protein kinase (MAPK) pathways.

MATERIALS AND METHODS

Ethics statement

The collection of human embryos was approved by the Medical Ethics Committee of Shengjing Hospital affiliated to China Medical University (approval ID: 2024PS1178K). Written informed consent was obtained from all donors before termination of pregnancy and tissue collection. All animal procedures were conducted according to the protocols approved by the Institutional Animal Care and Use Committee of Shenyang Agricultural University (approval ID: 202106038).

Sample collection

Five tetrapod species were examined in this study, including human (*Homo sapiens*), mouse (*Mus musculus*), Chinese soft-shelled turtle (*Pelodiscus sinensis*), chicken (*Gallus gallus*), and African clawed frog (*Xenopus laevis*). Human (CS16, 20, and 21), mouse (E10–13), turtle (TK13–18), chicken (S25–30), and frog (S53–55) embryos were used for sequence acquisition, whole-mount *in situ* hybridization, and skeletal staining. Chicken embryos were additionally used for *Zic3* overexpression experiments, RNA sequencing (RNA-seq), and real-time quantitative reverse transcription polymerase chain reaction (RT-qPCR). Staging criteria for human embryos were retrieved from the UNSW Embryology resource (https://embryology.med.unsw.edu.au/embryology/index.php/Main_Page), while staging systems for the remaining species were sourced from previous studies (Hamburger & Hamilton, 1951; Shan et al., 2023; Tokita & Kuratani, 2001; Wanek et al., 1989). Human embryos were collected at Shengjing Hospital of China Medical University (Shenyang, China), none of which exhibited developmental abnormalities. ICR mice were purchased from Liaoning Changsheng Biological Company (Shenyang, China) and were bred and mated in a controlled animal facility at 18–23°C with 50%–70% humidity. Fertilized turtle eggs were purchased from Jizhou District Huayu Turtle Farm (Tianjin, China) and incubated in moist sand at 30–32°C. Fertilized specific pathogen-free (SPF) chicken eggs were purchased from Beijing Merial Vital Laboratory Animal Technology Company (China) and incubated at 37.8°C and 60% humidity, with the eggs turned every 2h. Adult African clawed frogs were purchased from a local aquarium market (Shenyang, China) and bred and mated in a breeding tank at a water temperature of 23°C. Fertilized eggs were subjected to alternating light cycles using a biological lamp.

Whole-mount *in situ* hybridization (WISH)

Total RNA was extracted from the embryos of all species using a RNeasy Plus Mini Kit (Qiagen, Germany) and used to synthesize cDNA with a PrimeScript II 1st Strand cDNA Synthesis Kit (Taraka, China). Probes were amplified by PCR using cDNA templates, designed primers (Supplementary Table S1) and TransStart FastPfu DNA Polymerase (TransGen, China). PCR products were purified using a TIANquick Midi Purification Kit (Tiangen, China) and cloned into the pGEM-T vector (Promega, USA). Sense and antisense probes labeled with digoxigenin (DIG, Roche, Switzerland) were prepared by linearizing plasmids with restriction endonucleases (NEB, USA) and transcribing with SP6/T7 polymerase (Roche, Switzerland).

WISH was performed following previously published protocols (Hargrave et al., 2006). Embryos were fixed overnight in 4% paraformaldehyde (PFA), dehydrated in a methanol gradient, and stored at −80°C. Prior to hybridization, embryos were rehydrated in a methanol gradient. Embryos were then incubated with 10 μg/mL proteinase K, with turtle embryos requiring a 0.2 mol/L HCl treatment to enhance tissue permeability. Following digestion, embryos were washed in phosphate-buffered saline with Tween-20 (PBST), refixed in 0.2% glutaraldehyde in 4% PFA, and transferred to preheated hybridization solution with 1–2 μg/mL DIG-labeled probes, followed by overnight incubation at 65°C. After hybridization, embryos were washed, treated with blocking solution, and incubated overnight with alkaline phosphatase-coupled anti-DIG antibodies. The antibodies were then removed, and the washed embryos were incubated in NTMT containing NBT-BCIP (Roche, Switzerland) or BM-purple (Roche, Switzerland). The reaction was stopped when the appropriate color was achieved, and embryos were washed at least six times overnight in 1% Triton X-100 solution to reduce background staining. Finally, embryos were fixed in 4% PFA and imaged using a Leica microscope (M165FC, Germany).

Skeletal staining

Skeletal preparations were conducted in accordance with previous studies (Nagy et al., 2009; Ovchinnikov, 2009). For cartilage, embryonic limbs were dissected in PBS and fixed in Bouin's solution. Samples were washed in 75% ethanol containing 0.1% ammonia until residual yellow coloration was removed, equilibrated in 5% acetic acid, and stained with Alcian Blue until optimal contrast was achieved. After washing in methanol, the samples were stored in benzyl alcohol-benzyl benzoate until the tissue became transparent. For dual cartilage and bone staining, embryonic limbs were dissected in PBS and the skin was removed. After overnight fixation in 95% ethanol, the samples were transferred to acetone for overnight incubation, stained with Alcian Blue and Alizarin Red to appropriate colors, and finally stored in 1% KOH until transparency was achieved.

X-ray imaging

X-ray images of adult human and chicken limbs were acquired using a Mikasa X-ray machine (HF100H, Japan) at the Puppy Town Animal Hospital (Panjin, China). X-ray images of adult mouse, turtle, and frog limbs were acquired using a Runyes dental X-ray machine (RAY98P, China) at Doctor Chong Animal Hospital (Jinzhou, China).

Zic3 overexpression and interference

Coding sequences of human, mouse, and chicken *Zic3* genes (h*ZIC3*, m*Zic3*, and c*Zic3*, respectively), along with a *GFP* control sequence, were amplified and cloned into restriction endonuclease cleavage sites of the RCAS retroviral vector.

The *GFP* and RCAS constructs were generous gifts from Dr. Clifford J. Tabin. Details on NCBI accession numbers, primer sequences, and restriction endonuclease sites are available in Supplementary Figure S1. To silence c*Zic3*, a short hairpin RNA (sh-c*Zic3*) and a negative control (sh-NC) were designed and cloned downstream of the U6 promoter in RCAS to generate RCAS-sh-c*Zic3* and RCAS-sh-NC vectors, respectively.

Generation of the RCAS virus from DF-1 chicken fibroblasts was performed according to a previous protocol (Ahronian & Lewis, 2014). Briefly, DF-1 cells (Procell Life Science Company, CL-0279, China) were cultured in Dulbecco's Modified Eagle Medium (DMEM, Procell, China) supplemented with 10% fetal bovine serum (FBS, Sangon Biotech, China) and 1% penicillin/streptomycin (Sangon Biotech, China), and maintained at 39°C in a 5% CO_2 incubator. RCAS-*Zic3*, RCAS-*GFP*, and RCAS vectors were transfected into DF-1 cells using FuGENE®6 Transfection Reagent (Promega, USA). Supernatants were collected on days 15–17 post-transfection, filtered through a 0.45 μm filter, and centrifuged using an Optima XPN ultracentrifuge (Beckman Coulter, USA) at 50 000 ×*g* for 3.5 h at 4°C. Viral preparations were aliquoted and stored at −80°C until use.

Microinjection into developing chicken embryos was carried out as described previously (Gordon et al., 2009). Briefly, eggs at stage 10 (S10, 1.5 days) or stage 20 (S20, 3.5 days) were prepared by aspirating 2 mL of albumin from the yolk. A small "window" was cut in the eggshell surface, and 0.2–0.3 μL of virus solution containing fast green dye was microinjected (Eppendorf, Germany) into the expected fore- and hindlimb regions (lateral plate mesoderm, LPM) at S10 and anterior or posterior regions of the limb buds at S20. Post-injection, embryos were sealed with sterile plastic film and tape and returned to the incubator for continued development until the desired stage.

RT-qPCR

Total RNA was extracted from the zeugopods and autopods of the hindlimb buds of h*ZIC3*-overexpressing and RCAS-injected controls using a RNeasy Plus Mini Kit (Qiagen, Germany). cDNA was synthesized from the RNA using a PrimeScript™ RT Kit (Takara, China). Three independent RT-qPCR experiments were performed using TB Green® Premix Ex Taq™ II (Takara, China) on a real-time PCR detection system (LightCycler® 96, Roche, Switzerland). *TBP* was used as the internal control, and relative mRNA levels were calculated using the $2^{-\Delta\Delta Ct}$ formula (Livak & Schmittgen, 2001). Primers used for RT-qPCR are listed in Supplementary Table S2.

***In vitro* differentiation assays**

The osteoblast differentiation level assay was performed following a previously published study (Fu et al., 2016). In brief, HEK293T cells (Procell, China) were cultured in DMEM (Procell, China) supplemented with 10% FBS (Procell, China), while human mesenchymal stem cells from the umbilical cord matrix (UCM-hMSCs, Yocon, China) were cultured in serum-free mesenchymal stem cell basal medium (Yocon, China). Both cell types were maintained in a humidified incubator at 37°C with 5% CO_2. The full-length human *Zic3* gene was inserted into the pCDH-MSCV-MSC-EF1-copGFP-T2A-Puro vector (TranSheep Shanghai, China). The lentiviral vector carrying human *Zic3*, along with two helper vectors, was transfected into HEK293T cells. Virus supernatants were collected at 72 h post-transfection, filtered and concentrated for infection of UCM-hMSCs. When their density reached approximately 80%, cells were dissociated using 0.25% trypsin and 0.04% EDTA (Sangon, China) and seeded into 6-well plates for osteogenic induction experiments. Osteogenic differentiation of UCM-hMSCs was induced using a Human Umbilical Cord Mesenchymal Stem Cell Osteogenic Differentiation Medium Kit (Cyagen, China), following the manufacturer's instructions. After 3 weeks of induction, cells were washed with PBS, fixed with 4% PFA for 30 min, and stained with Alizarin Red staining solution for 10 min. Images were collected using a Leica microscope (Germany).

RNA-seq and data analysis

A total of 20 hindlimb samples, including zeugopods and autopods, were collected from 10 chick embryos: five subjected to h*ZIC3* overexpression and five RCAS-infected controls. Embryos were injected at S10 and collected at S30. Total RNA was extracted using a RNeasy Plus Mini Kit (Qiagen, Germany), and RNA concentration and purity were assessed using a Qubit fluorometer (Life Technologies, USA) and Nanodrop spectrophotometer (Thermo, USA). RNA integrity was evaluated using an Agilent Bioanalyzer 2100 (Agilent Technologies, USA). For each sample, 3 μg of high-quality total RNA was used as input material for library construction. Libraries were commercially sequenced (Novogene Biotech, China) using the Illumina NovaSeq 6000 platform (Illumina, USA). Each library yielded approximately 30 million 150 bp paired-end reads.

Raw reads were mapped to the NCBI *Gallus gallus* reference genome (bGalGal1.mat.broiler.GRCg7b) with an inserted h*Zic3* cDNA sequence using Hisat2 (v.2.2.1.) (Pertea et al., 2016). Transcript abundance was quantified in transcripts per million (TPM) to standardize for sequencing depth and transcript length. TPM values were used for pairwise Pearson correlation analysis and principal component analysis (PCA). Correlation heatmaps were generated using the pheatmap package (v.1.0.12). Datasets were *Z*-score-standardized before PCA analysis using the "prcomp" function in R. Differential expression analysis was performed using the DESeq2 package (v.1.42.0) (Love et al., 2014). Genes with *P*-adjust<0.05 and $|\log_2 FoldChange| \geq 0.6$ were defined as differentially expressed genes (DEGs). Gene Ontology (GO) and Kyoto Encyclopedia of Genes and Genomes (KEGG) enrichment analyses were performed using the Database for the Annotation, Visualization, and Integrated Discovery (DAVID, v.2024q1, https://david.ncifcrf.gov/) (Huang et al., 2009; Sherman et al., 2022). Significant thresholds were set to $P<0.05$. Gene set enrichment analysis (GSEA) was performed using the OmicStudio tool (https://www.omicstudio.cn/tool).

Statistical analysis

All results shown are representative expression patterns obtained by analyzing at least three independent samples per probe, except for the expression of *Zic3* in the human limb bud at CS16 (two samples). Experimental data are reported as mean±standard deviation (SD) of at least three independent samples. Data were analyzed using two-tailed unpaired *t*-test. *P*-values less than 0.05 were considered significant. *: $P<0.05$; **: $P<0.01$; ***: $P<0.001$.

RESULTS

***Zic3* expression in tetrapod limb buds**

To compare the expression of *Zic3* across tetrapods, two

developmental stages were selected for five species (human, mouse, chicken, Chinese soft turtle, and African clawed frog) based on limb bud morphology and the timing of skeletal patterning revealed by cartilage staining. The early stage corresponded to AP expansion, while the late stage marked the initial digit formation within the autopod. WISH revealed that *Zic3* exhibited a conserved anterior expression pattern during the early stage in both fore- and hindlimb buds across all examined species (Figure 1). In particular, robust anterior expression was observed in regions corresponding to the presumptive digits I and II. In human embryos, which were slightly larger in size than those of the other species, the expression of *Zic3* was more proximal (restricted from the distal tip). The spatial distribution of *Zic3* aligned with early digit patterning territories, suggesting a regulatory role in anterior limb bud development. A comparable anterior *Zic3* expression pattern was also observed in the pectoral fin buds of *Scyliorhinus canicula*, supporting evolutionary conservation of *Zic3* expression from fins to limbs (Onimaru et al., 2015). As digit morphogenesis progressed, *Zic3* expression in the tetrapod limbs differentiated. At the late stage, *Zic3* exhibited strong expression at the proximal base of the DI metacarpals and metatarsals in humans, and at the proximal regions of the DI metacarpals and metatarsals and adjacent posterior interdigital mesenchyme in both mice and turtles. In frog hindlimbs and chicken fore- and hindlimbs, *Zic3* expression remained elevated in the DI region, whereas no expression was detected in the frog forelimb, potentially reflecting evolutionary loss of DI. Across tetrapods, *Zic3* expression showed an inverse correlation with anterior digit length during both embryonic and adult stages (Figure 1). In humans, for instance, DI metacarpals and metatarsals—domains of high *Zic3* expression—are markedly shorter than those of the other digits. Based on these observations, we hypothesized that *Zic3* may restrict anterior digit elongation, which was further tested through functional analyses.

***Zic3* overexpression and interference experiments**

To elucidate the functional role of *Zic3* in limb development, RCAS-based avian retroviral vectors were employed to overexpress h*ZIC3*, m*Zic3*, and c*Zic3* and knockdown c*Zic3* expression in chicken embryo limbs. RCAS-GFP and empty RCAS vectors served as negative controls. Embryos infected with *GFP* exhibited strong fluorescence in targeted limbs without detectable morphological differences compared to uninjected contralateral limbs (Supplementary Figure S2). To evaluate the *in vivo* efficacy of c*Zic3* knockdown, RCAS-sh-c*Zic3* virus was microinjected into the anterior region of limb buds at S20. Embryos were collected at S30, with uninjected contralateral limbs used as internal controls. Quantitative analysis confirmed that c*Zic3* transcript levels were significantly reduced in both forelimbs and hindlimbs following RCAS-sh-c*Zic3* infection (Supplementary Figure S1). Despite effective gene silencing, no overt morphological alterations were observed in the chicken embryos at S35.

In contrast, overexpression of h*ZIC3*, m*Zic3*, and c*Zic3* in chicken embryos (via RCAS injection into the right limb at S10) resulted in pronounced limb shortening compared to the uninfected left limb and *GFP*/RCAS infected controls (Figure 2A, B; Supplementary Figure S1, S2). The reduction in limb length affected all major segments, including the stylopod, zeugopod, and autopod, of both fore- and hindlimbs. Notably, despite significant skeletal shortening and delayed ossification, no bone elements were lost. Targeted overexpression of h*ZIC3* in the posterior region of the limb buds induced localized morphological defects compared to the contralateral limb buds, characterized by a shortening of the second and third digits of the forelimbs and third and fourth toes of the hindlimbs, as well as a significant delay in ossification (Figure 2C). RT-qPCR analysis revealed significantly increased h*ZIC3* mRNA expression but no significant change in c*Zic3* expression in the infected chicken limbs (Figure 2D), confirming that h*ZIC3* is transcriptionally

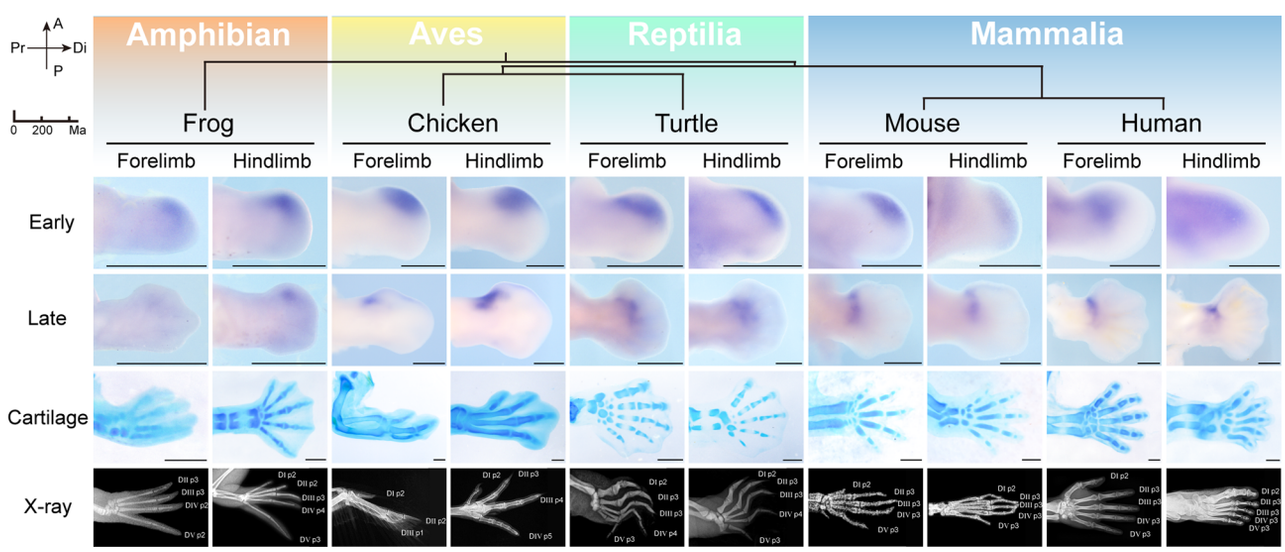

Figure 1 *Zic3* expression and skeletal phenotypes across tetrapod limbs

Developmental stages examined for early limb bud morphology were as follows: Human (*Homo sapiens*), Carnegie stage (CS) 16; mouse (*Mus musculus*), embryonic day (E) 10; turtle (*Pelodiscus sinensis*), Tokita-Kuratani stage (TK) 13; chicken (*Gallus gallus*), stage (S) 25; frog (*Xenopus laevis*), S53. Late-stage expression was assessed at human CS20; mouse E12; turtle TK17; chicken S28; and frog S54. Cartilage staining was performed at human CS21; mouse E13; turtle TK18; chicken S30; and frog S55. X-ray images show adult digits (D) and number of phalanges (p). All limb images are oriented dorsally with anterior positioned upward and distal toward the right. A, anterior; P, posterior; Pr, proximal; Di, distal. Scale bar: 0.5 mm. Top: Time tree displays evolutionary relationships among species. Ma, million years ago (Kumar et al., 2022).

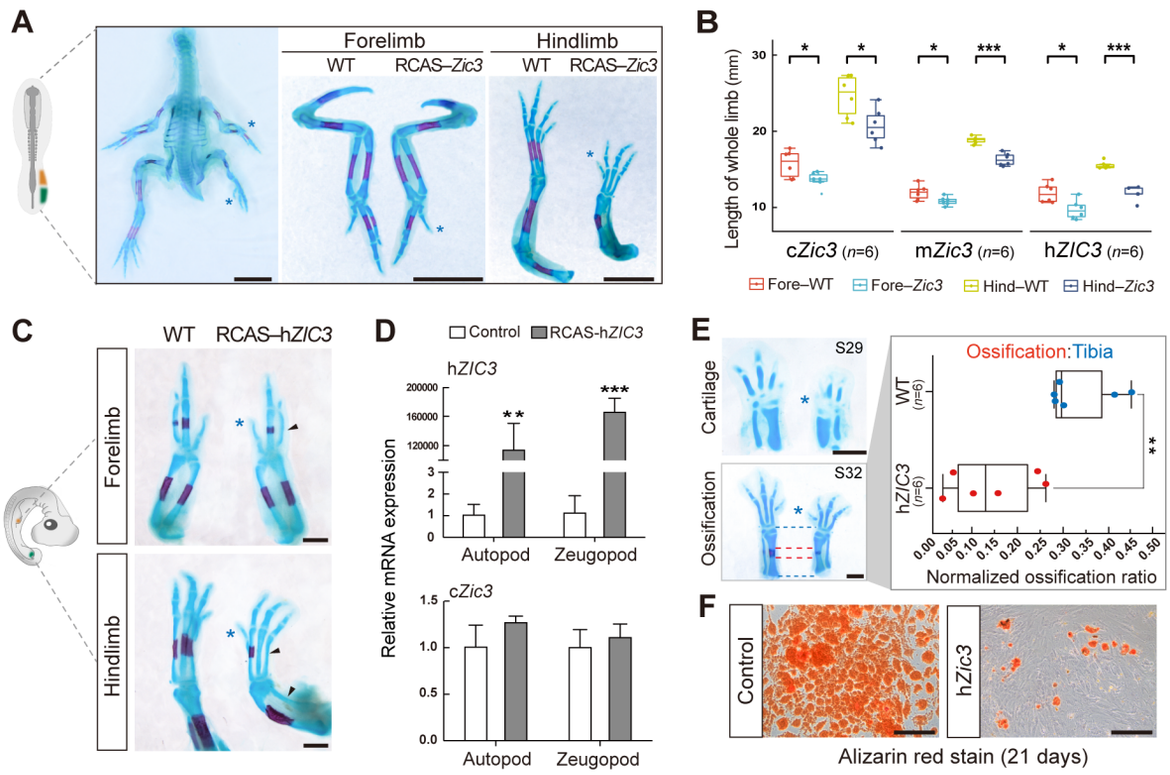

Figure 2 Effects of *Zic3* overexpression on skeletal development

A: Skeletal staining of h*ZIC3*-overexpressing chicken embryos injected at S10 and collected at S35. Scale bar: 0.5 cm. B: Quantification of limb length in h*ZIC3*-, m*Zic3*-, and c*Zic3*-overexpressing chicken embryos injected at S10 and collected at S35. C: Skeletal staining of h*ZIC3*-overexpressing chicken embryos injected at S20 and collected at S35. Right limb was infected with RCAS-h*ZIC3*, while left limb served as an uninfected control. Scale bar: 1 mm. Model diagrams in A and C show injection locations. Orange, target area of forelimb; green, target area of hindlimb. D: RT-qPCR analysis of h*ZIC3*-overexpressing chicken limb buds injected at S10 and collected at S35 (n=3). E: Skeletal staining of h*ZIC3*-overexpressing chicken embryos injected at S10 and collected at S29/32 and normalized ossification ratio at S32. Red/blue dashed lines indicate ossification range/tibia length. Scale bar: 1 mm. Box plots represent the median, quartile partition, range, and individual biological replicates. F: Osteogenic induction of UCM-hMSCs. Scale bar: 200 μm. *: P<0.05; **: P<0.01; ***: P<0.001. All limb images are shown in dorsal view, with a blue asterisk marking DI.

and functionally active in the chicken embryonic limb.

To examine the role of *Zic3* in limb skeletal development, embryos overexpressing h*ZIC3* (injected at S10) were collected at various developmental stages, spanning early cartilage formation to limb ossification, and subjected to skeletal staining. Overexpression of h*ZIC3* resulted in marked delays in both ossification of the limbs and chondrogenesis (Figure 2E). Compared to the uninjected contralateral side, h*ZIC3*-overexpressing hindlimbs exhibited delayed chondrogenesis in DI and DII, delayed cartilage condensation in DIII and DIV, shortening of the tibia and fibula at S29, and delayed tibial ossification at S32. To determine whether the impaired ossification was a consequence of delayed cartilage maturation or reflected a direct influence on endochondral ossification processes, the ratio of ossified tissue length to total tibial length was quantified between injected and contralateral limbs. This analysis revealed a significant reduction in the ossification ratio, indicating that *Zic3* specifically impedes ossification beyond what would be expected from proportional limb shortening alone (Figure 2E). Additionally, overexpression of h*ZIC3* during *in vitro* osteogenic induction of UCM-hMSCs resulted in suppressed ossification of human cells (Figure 2F), indicating a conserved inhibitory role for *Zic3* in bone development across both humans and chickens.

RNA-seq analysis of *Zic3*-overexpressing limbs

To define the molecular pathways through which *Zic3* influences the regulation of limb development, RNA-seq was performed on zeugopod and autopod tissues from chicken hindlimbs infected with RCAS-h*ZIC3* or RCAS control (injected at S10 and collected at S30, Figure 3A). Hierarchical cluster analysis (HCA) and PCA of transcriptomic profiles identified four distinctive gene expression clusters, each consistently reproduced across five biological replicates (Figure 3B), confirming the robustness and reproducibility of the transcriptional responses. Differential expression analysis identified 963 and 551 DEGs in the zeugopod and autopod, respectively (Figure 3C; Supplementary Figure S3A), with 283 DEGs shared between the two regions (Supplementary Figure S3A). The zeugopod exhibited a greater number of DEGs and a broader range of enriched GO categories compared to the autopod (Supplementary Figure S3B). GO Biological Process (GO-BP) analysis of DEGs revealed significant down-regulation of categories related to ossification, cartilage development, and osteoblast differentiation (Figure 3D), suggesting that *Zic3* overexpression inhibits the skeletal development of limbs. KEGG analysis of the down-regulated genes identified five enriched pathways implicated in skeletal development (Brachvogel et al., 2013; Chen et al., 2023; Salhotra et al., 2020). ECM-receptor interaction and FA pathways were enriched in both limb segments, while the HH,

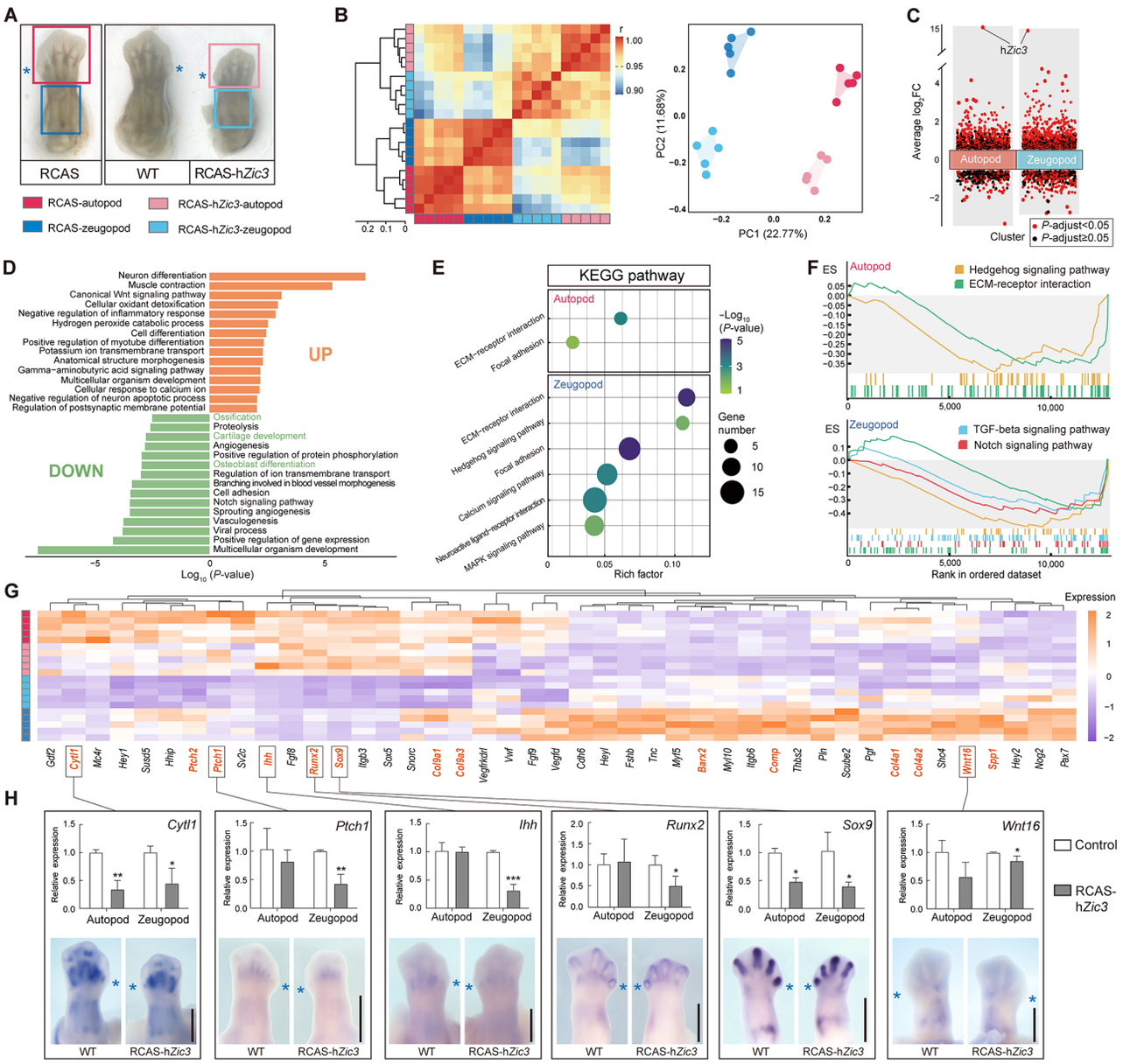

Figure 3 RNA-seq analysis and validation of DEGs in h*ZIC3*-overexpressing limbs

A: Representative images of hindlimb overexpressing RCAS-h*ZIC3*, contralateral wild-type (WT) limb, and RCAS-injected controls. Colored lines indicate dissection protocol used to obtain RNA-seq samples. B: HCA and PCA of transcriptomes from five biological replicates per group. C: Group volcano plots of DEGs following h*ZIC3* overexpression. D: Top 15 enriched GO-BP terms for up- and down-regulated DEGs. Three skeletal development-related terms are highlighted in green. E: KEGG enrichment analysis of down-regulated DEGs in autopod and zeugopod. F: GSEA showing pathway suppression in both limb segments. G: Heatmap of DEGs enriched in GO-BP terms related to skeletal development. RT-qPCR-validated genes are highlighted in orange. Colors used for samples are the same as in (A, B, and G). H: RT-qPCR and WISH analysis of six down-regulated DEGs. n=3; Scale bar: 1 mm; *: P<0.05; **: P<0.01; ***: P<0.001. All limb images are shown in dorsal view, with blue asterisk marking DI.

calcium, and MAPK signaling pathways were enriched in the zeugopod (Figure 3E). GSEA showed a significant attenuation of the HH signaling pathway and ECM-receptor interactions in the zeugopod and autopod (Figure 3F; Supplementary Figure S4A, B), as well as additional down-regulation of the Notch and TGF-β signaling pathways, canonical regulators of cartilage and bone development (Dexheimer et al., 2016; White et al., 2015), in the zeugopod (Figure 3F; Supplementary Figure S4C, D). These regional differences may reflect the more advanced developmental state and higher degree of differentiation in the zeugopod relative to the autopod at this stage.

Based on the enriched GO-BP terms related to skeletal development, 14 down-regulated genes were selected for RT-qPCR validation, including *Cytl1*, *Ptch1*, *Ptch2*, *Ihh*, *Runx2*, *Sox9*, *Col9a1*, *Col9a3*, *Barx2*, *Comp*, *Col4a1*, *Col4a2*, *Wnt16*, and *Spp1* (Figures 3G, 4A). WISH was performed for six pivotal regulators (*Cytl1*, *Sox9*, *Ihh*, *Ptch1*, *Runx2*, and *Wnt16*) to visualize spatial expression changes (Gao et al., 2009; Wang et al., 2022; Ye & Liu, 2022; Zhu et al., 2019). In addition, RT-qPCR also validated the up-regulation of six genes, including *Cryab*, which stabilizes β-catenin, and *Casq2*, *Des*, *Myl2*, *Tnmd*, and *Tnni1*, which are associated with muscle and tendon development (Amthor et al., 2002; Liu et al., 2015; Michelucci et al., 2022; Sheikh et al., 2015; Sheng & Jin, 2016). All validation experiments were performed on

samples developmentally matched to the RNA-seq timepoint. The observed expression trends were consistent with the RNA-seq results, supporting the reliability of the transcriptomic dataset (Figures 3H, 4A, B). Given the reported interactions among *Zic3*, *Gli3*, and *Shh* during early limb development (Quinn et al., 2012), the expression levels of *Gli3* and *Shh* in the limbs of h*ZIC3*-overexpressing embryos were examined at S30. Furthermore, considering their expression during the early limb development period, the expression levels of *Gli3* and *Shh* in the limbs of wild-type and h*ZIC3*-overexpressing chicken embryos were examined at S25. However, no significant changes in expression were observed (Figure 4C).

DISCUSSION

Zic3 functions as an upstream regulator of transcription factors that mediate cell fate transitions and promote differentiation (Yang et al., 2019). In this study, *Zic3* expression in limb buds was observed prior to the onset of chondrogenesis. Following *Zic3* overexpression, GO-BP enrichment analysis of DEGs revealed significant enrichment of terms related to cell differentiation and regulation of transcription by RNA polymerase II promoter (Supplementary Figure S3B), consistent with a regulatory role at early developmental stages. These results suggest that *Zic3* may delay cell differentiation and attenuate the transcription of genes associated with growth and development, thereby contributing to slower anterior development relative to posterior regions. This inhibitory effect was observed from early limb bud stages through the emergence of reduced tarsal-metatarsal and carpal-metacarpal elements, aligning with the dynamic spatiotemporal pattern of *Zic3* expression. Functional data also indicated that *Zic3* does not disrupt core skeletal morphogenetic pathways but rather modulates intrinsic regulatory networks controlling bone patterning. Infections targeting the entire limb or restricted regions produced a consistent phenomenon —characterized by skeletal shortening —without generating a new limb component phenotype. This supports the hypothesis that the inhibitory effect of *Zic3* on bone progression may be an indirect effect similar to transcriptional repression.

Limb development is a complex biological process involving tightly coordinated signaling interactions and gene expression programs (Petit et al., 2017). The Zic3 protein has been shown to interact physically with Gli3 via its N-terminal zinc finger domain and to affect the *Gli3* (+/−) phenotype but not the *Gli3* (−/−) phenotype (Quinn et al., 2012). Despite this known interaction, *Zic3* overexpression in the chick limb buds did not alter *Gli3* or *Shh* expression. One possible explanation is that in wild-type limb development, *Zic3* may competitively bind to GLI target genes in the anterior region, participating in the regulation of skeletal development. Additionally, *Zic2*, a paralog from the same family, has been reported to act as a transcriptional co-regulator by interacting with *TCF4* repression domains without interfering with *TCF4* DNA-binding ability (Pourebrahim et al., 2011). A comparable regulatory strategy may also apply to *Zic3* and warrants further investigation. *In vivo* knockdown of *Zic3* failed to induce gross limb abnormalities, consistent with findings from *Zic3*-null mice (Quinn et al., 2012). This may be explained by compensatory functions within the *Zic* family, analogous to the functional

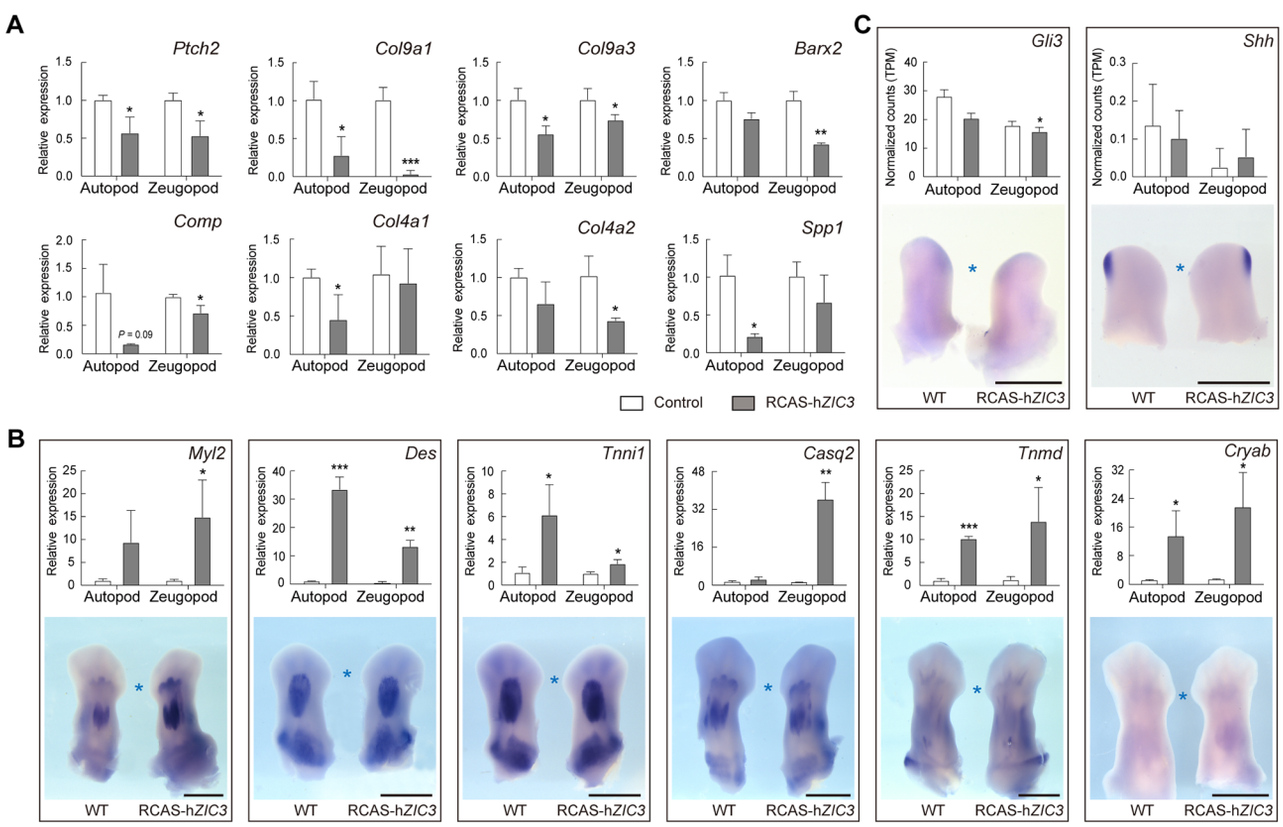

Figure 4 RT-qPCR and WISH validation of DEGs identified by RNA-seq

A: RT-qPCR validation of eight down-regulated genes. B: RT-qPCR and WISH validation of six up-regulated genes. C: RNA-Seq and WISH validation of *Gli3* and *Shh*. *n*=3. Scale bar: 1 mm; *: $P<0.05$; **: $P<0.01$; ***: $P<0.001$. All limb images are shown in dorsal view, with blue asterisk marking DI.

redundancy observed among *Hoxd* paralogs (*Hoxd10–13*) (Yakushiji-Kaminatsui et al., 2018), which serve to buffer developmental programs against perturbation.

In tetrapods, *Zic3* expression exhibits an inverse relationship with the developmental sequence of anterior digit formation (Montero et al., 2017). Given its capacity to suppress chondrogenesis and ossification, sustained and conserved expression of *Zic3* likely contributed to the delayed emergence and reduced length of DI, positioning it as the last-forming anterior digit (Figure 5A). The broader early expression of *Zic3* may also have contributed to the delayed development of DII. Furthermore, overexpression of *Zic3* was associated with a decrease in *Sox9* expression, a known marker gene of skeletal development. This observation aligns with the spatial patterning of *Sox9* during normal limb development, where DIV and DIII form earlier, and DI emerges last (Montero et al., 2017). With progressive limb development, *Zic3* expression became increasingly confined to the anterior margin, mirroring the AP axis shift that accompanied the evolutionary transition from fins to limbs (Onimaru et al., 2015; Woltering et al., 2020). In later stages, Zic3 expression was no longer detected in the frog forelimb, consistent with the evolutionary absence of DI and resulting developmental and morphological convergence of DII–DIV. In mouse and turtle limbs, late-stage *Zic3* expression domains were broader than those observed in chicken and frog,

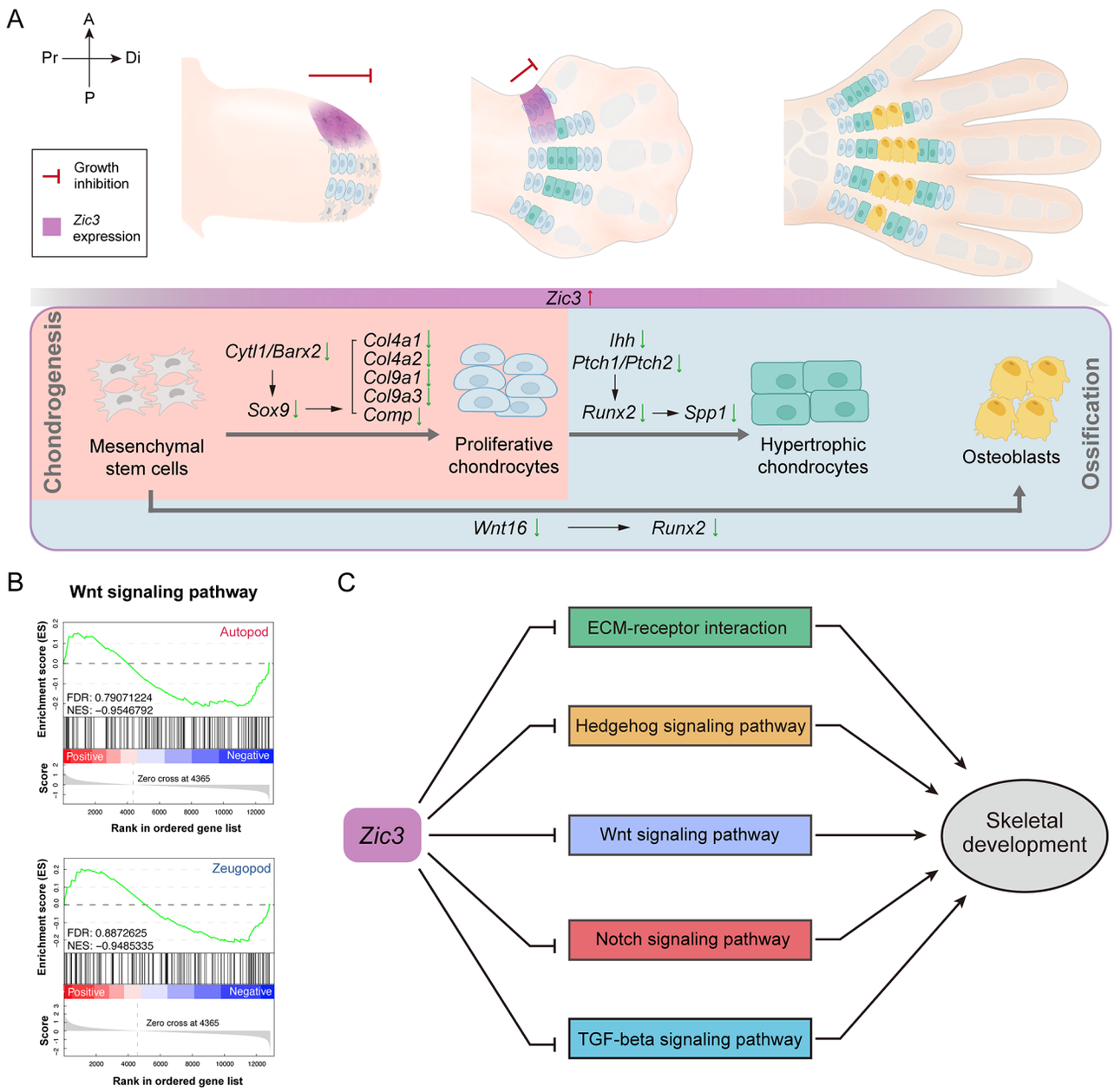

Figure 5 *Zic3* modulates digit patterning mechanisms during limb development

A: Schematic model illustrating the spatial dynamics of limb development and the influence of *Zic3* expression on anterior digit morphology. Dorsal side is shown. A, anterior; P, posterior; Pr, proximal; Di, distal. Altered expression of key skeletal regulators following *Zic3* overexpression is indicated by arrows next to gene names, with arrow direction denoting up- or downregulation. B: GSEA showing inhibition of the Wnt signaling pathway in the autopod and zeugopod following *Zic3* overexpression. C: Schematic summary of five signaling pathways suppressed by *Zic3* during limb development.

supporting the hypothesis that interspecific differences in skeletal morphology arise from variation in signaling landscapes (Varga & Varga, 2022). The broad expression of *Zic3* from amphibians to reptiles and mammals and its restricted expression in birds appears to reflect the functional divergence of limb structure, with greater skeletal flexibility in terrestrial taxa and the structural simplification of birds adapted for powered flight. These findings are consistent with the notion that the expression of the same gene has been repeatedly and finely modified across vertebrate taxa, benefiting the adaptation of different species to various environments (Swank et al., 2021).

This study revealed that *Zic3* regulates many genes and multiple key pathways in limb development. For example, among the validated down-regulated genes, *Cytl1* and *Barx2* both act upstream of *Sox9* through different pathways, ultimately controlling the expression of major cartilage matrix genes (*Col4a1*, *Col4a2*, *Col9a1*, and *Col9a3*) (Coricor & Serra, 2016; Meech et al., 2005; Shen et al., 2023; Zhu et al., 2019). These genes encode the core structural collagens of the cartilage ECM, with COL IV and COL IX forming scaffold networks critical for cartilage integrity. COL IX also interacts with Comp, facilitating matrix organization during chondrogenesis (Brachvogel et al., 2013). During endochondral ossification, *Runx2* induces chondrocyte proliferation via HH signaling (including *Ihh*, *Ptch1*, and *Ptch2*), while driving the expression of *Spp1* in hypertrophic chondrocytes, promoting chondrocyte maturation (Komori, 2022). *Wnt16* has been shown to promote osteoblast differentiation from periosteal cells by up-regulating *Runx2* expression (Ye & Liu, 2022). These regulatory cascades align with the phenotypes observed following *Zic3* overexpression, including delayed chondrogenesis, impaired endochondral ossification, and shortened cartilage and bone (Figure 5A). Previous studies have indicated that *Zic* proteins interfere with canonical Wnt signaling by binding TCF-β-catenin complexes and blocking downstream transcriptional activation (Yang et al., 2019; Zhao et al., 2019). In this study, *Cryab*, a gene known to stabilize β-catenin, was found to be up-regulated, and although overall Wnt pathway suppression in the zeugopod and autopod did not reach statistical significance, the trend was consistent with *Zic3*-mediated inhibition (Figure 5B). Crosstalk between the Wnt signaling pathway and ECM-receptor interaction, HH, Notch, and TGF-β signaling pathways orchestrates chondrocyte differentiation, osteoblast differentiation and skeletal development (Vlashi et al., 2023; Zhang et al., 2017). Our results demonstrated that overexpression of *Zic3* inhibited all these pathways during limb development, highlighting its central role in modulating the transcriptional network governing skeletal patterning (Figure 5C).

In summary, our transgenic-mediated overexpression experiments demonstrated that elevated *Zic3* expression in the forelimb bud region delayed the emergence and elongation of anterior digits. Persistent *Zic3* activity impaired chondrogenesis and endochondral ossification of the anterior meta-carpals/tarsals, ultimately contributing to the pronounced shortening of DI across tetrapods. Furthermore, based on RNA-seq data and DEG validation, our study unveiled downstream genes and pathways regulated by *Zic3*, including the suppression of various bone-related genes, potentially explaining why *Zic3* mutations lead to limb defects in human VACTERL/VATER syndrome (Thiem et al., 2022). Collectively, these findings not only enhance our understanding of limb morphogenesis but also provide new insights into the pathogenesis of *Zic3*-related diseases (e.g., OMIM#306955 and #314390). Future research should incorporate a variety of *in vitro* experimental methods, including functional inhibition of *Zic3* in limb skeletal progenitor cells and bone-specific conditional knockout techniques in mouse models, to further explore how *Zic3* regulates skeletal development. Such approaches should help clarify the regulatory interactions between *Zic3*, *Gli3*, and *Shh*, and reveal the role of *Zic3* in limb development, bone growth, and differentiation, as well as its role in broader regulatory networks.

DATA AVAILABILITY

The RNA-seq data generated in this study have been deposited in the Gene Expression Omnibus (GEO) database (accession number GSE266376), Genome Sequence Archive (GSA) database (https://ngdc.cncb.ac.cn/gsa/) (accession number PRJCA038329), and Science Data Bank (doi: 10.57760/sciencedb.j00139.00196).

SUPPLEMENTARY DATA

Supplementary data to this article can be found online.

COMPETING INTERESTS

The authors declare that they have no competing interests.

AUTHORS' CONTRIBUTIONS

Z.W., S.S.L., and S.B.B. designed the study. S.S.L., S.B.B., J.L., and Y.N.T. analyzed the data. X.F.S., C.H.Y., and S.Y.S. acquired the data; Z.Q.J. and X.P.L. verified the data. S.S.L., S.B.B., Z.W., and J.L. wrote the manuscript. J.L., Z.W., and D.M.I. reviewed the manuscript. All authors read and approved the final version of the manuscript.

REFERENCES

Ahronian LG, Lewis BC. 2014. Generation of high-titer RCAS virus from DF1 chicken fibroblasts. *Cold Spring Harbor Protocols*, **2014**(11): 1161–1166.

Amthor H, Huang RJ, McKinnell I, et al. 2002. The regulation and action of myostatin as a negative regulator of muscle development during avian embryogenesis. *Developmental Biology*, **251**(2): 241–257.

Bastida MF, Pérez-Gómez R, Trofka A, et al. 2020. The formation of the thumb requires direct modulation of *Gli3* transcription by Hoxa13. *Proceedings of the National Academy of Sciences of the United States of America*, **117**(2): 1090–1096.

Brachvogel B, Zaucke F, Dave K, et al. 2013. Comparative proteomic analysis of normal and collagen IX null mouse cartilage reveals altered extracellular matrix composition and novel components of the collagen IX interactome. *Journal of Biological Chemistry*, **288**(19): 13481–13492.

Cao JY, Spielmann M, Qiu XJ, et al. 2019. The single-cell transcriptional landscape of mammalian organogenesis. *Nature*, **566**(7745): 496–502.

Chen S, He TL, Zhong YM, et al. 2023. Roles of focal adhesion proteins in skeleton and diseases. *Acta Pharmaceutica Sinica B*, **13**(3): 998–1013.

Chiang C, Litingtung Y, Harris MP, et al. 2001. Manifestation of the limb prepattern: limb development in the absence of sonic hedgehog function. *Developmental Biology*, **236**(2): 421–435.

Coricor G, Serra R. 2016. TGF-β regulates phosphorylation and stabilization of Sox9 protein in chondrocytes through p38 and Smad dependent mechanisms. *Scientific Rreports*, **6**: 38616.

Dexheimer V, Gabler J, Bomans K, et al. 2016. Differential expression of TGF-β superfamily members and role of Smad1/5/9-signalling in chondral versus endochondral chondrocyte differentiation. *Scientific Reports*, **6**: 36655.

Fu XJ, Yang HL, Zhang H, et al. 2016. Improved osteogenesis and upregulated immunogenicity in human placenta-derived mesenchymal stem cells primed with osteogenic induction medium. *Stem Cell Research & Therapy*, **7**: 138.

Gao B, Hu JX, Stricker S, et al. 2009. A mutation in *Ihh* that causes digit abnormalities alters its signalling capacity and range. *Nature*, **458**(7242): 1196–1200.

Gordon CT, Rodda FA, Farlie PG. 2009. The RCAS retroviral expression system in the study of skeletal development. *Developmental Dynamics*, **238**(4): 797–811.

Hamburger V, Hamilton HL. 1951. A series of normal stages in the development of the chick embryo. *Journal of Morphology*, **88**(1): 49–92.

Hargrave M, Bowles J, Koopman P. 2006. *In situ* hybridization of whole-mount embryos. *In*: Darby IA, Hewitson TD. In Situ Hybridization Protocols. 3rd ed. Humana Totowa: Springer, 103–113.

Hilger AC, Halbritter J, Pennimpede T, et al. 2015. Targeted resequencing of 29 candidate genes and mouse expression studies implicate *ZIC3* and *FOXF1* in human VATER/VACTERL association. *Human Mutation*, **36**(12): 1150–1154.

Huang DW, Sherman BT, Lempicki RA. 2009. Systematic and integrative analysis of large gene lists using DAVID bioinformatics resources. *Nature Protocols*, **4**(1): 44–57.

Inoue T, Ota M, Mikoshiba K, et al. 2007. *Zic2* and *Zic3* synergistically control neurulation and segmentation of paraxial mesoderm in mouse embryo. *Developmental Biology*, **306**(2): 669–684.

Komori T. 2022. Whole aspect of Runx2 functions in skeletal development. *International Journal of Molecular Sciences*, **23**(10): 5776.

Kumar S, Suleski M, Craig JM, et al. 2022. TimeTree 5: an expanded resource for species divergence times. *Molecular Biology and Evolution*, **39**(8): msac174.

Litingtung Y, Dahn RD, Li YN, et al. 2002. *Shh* and *Gli3* are dispensable for limb skeleton formation but regulate digit number and identity. *Nature*, **418**(6901): 979–983.

Liu H, Xu JY, Liu CF, et al. 2015. Whole transcriptome expression profiling of mouse limb tendon development by using RNA‐seq. *Journal of Orthopaedic Research*, **33**(6): 840–848.

Livak KJ, Schmittgen TD. 2001. Analysis of relative gene expression data using real-time quantitative PCR and the $2^{-\Delta\Delta CT}$ method. *Methods*, **25**(4): 402–408.

Love MI, Huber W, Anders S. 2014. Moderated estimation of fold change and dispersion for RNA-seq data with DESeq2. *Genome Biology*, **15**(12): 550.

McQueen C, Towers M. 2020. Establishing the pattern of the vertebrate limb. *Development*, **147**(17): dev177956.

Meech R, Edelman DB, Jones FS, et al. 2005. The homeobox transcription factor Barx2 regulates chondrogenesis during limb development. *Development*, **132**(9): 2135–2146.

Michelucci A, Pietrangelo L, Rastelli G, et al. 2022. Constitutive assembly of Ca^{2+} entry units in soleus muscle from calsequestrin knockout mice. *Journal of General Physiology*, **154**(12): e202213114.

Montero JA, Lorda-Diez CI, Francisco-Morcillo J, et al. 2017. *Sox9* expression in amniotes: species-specific differences in the formation of digits. *Frontiers in Cell and Developmental Biology*, **5**: 23.

Nagy A, Gertsenstein M, Vintersten K, et al. 2009. Alcian blue staining of the mouse fetal cartilaginous skeleton. *Cold Spring Harbor Protocols*, **2009**(3): pdb. prot5169.

Oberg KC. 2014. Review of the molecular development of the thumb: digit primera. *Clinical Orthopaedics and Related Research*, **472**(4): 1101–1105.

Onimaru K, Kuraku S, Takagi W, et al. 2015. A shift in anterior-posterior positional information underlies the fin-to-limb evolution. *eLife*, **4**: e07048.

Ovchinnikov D. 2009. Alcian blue/alizarin red staining of cartilage and bone in mouse. *Cold Spring Harbor Protocols*, **2009**(3): pdb. prot5170.

Panman L, Drenth T, Tewelscher P, et al. 2005. Genetic interaction of *Gli3* and *Alx4* during limb development. *The International Journal of Developmental Biology*, **49**(4): 443–448.

Pertea M, Kim D, Pertea GM, et al. 2016. Transcript-level expression analysis of RNA-seq experiments with HISAT, stringtie and ballgown. *Nature Protocols*, **11**(9): 1650–1667.

Petit F, Sears KE, Ahituv N. 2017. Limb development: a paradigm of gene regulation. *Nature Reviews Genetics*, **18**(4): 245–258.

Phillips HM, Stothard CA, Shaikh Qureshi WM, et al. 2019. *Pax9* is required for cardiovascular development and interacts with *Tbx1* in the pharyngeal endoderm to control 4th pharyngeal arch artery morphogenesis. *Development*, **146**(18): dev177618.

Pourebrahim R, Houtmeyers R, Ghogomu S, et al. 2011. Transcription factor Zic2 inhibits Wnt/β-catenin protein signaling. *Journal of Biological Chemistry*, **286**(43): 37732–37740.

Purandare SM, Ware SM, Kwan KM, et al. 2002. A complex syndrome of left-right axis, central nervous system and axial skeleton defects in *Zic3* mutant mice. *Development*, **129**(9): 2293–2302.

Quinn ME, Haaning A, Ware SM. 2012. Preaxial polydactyly caused by *Gli3* haploinsufficiency is rescued by *Zic3* loss of function in mice. *Human Molecular Genetics*, **21**(8): 1888–1896.

Salhotra A, Shah HN, Levi B, et al. 2020. Mechanisms of bone development and repair. *Nature Reviews Molecular Cell Biology*, **21**(11): 696–711.

Saxena A, Towers M, Cooper KL. 2017. The origins, scaling and loss of tetrapod digits. *Philosophical Transactions of the Royal Society B: Biological Sciences*, **372**(1713): 20150482.

Shan ZX, Li SS, Yu CH, et al. 2023. Embryonic and skeletal development of the albino African clawed frog (*Xenopus laevis*). *Journal of Anatomy*, **242**(6): 1051–1066.

Sheikh F, Lyon RC, Chen J. 2015. Functions of myosin light chain-2 (MYL2) in cardiac muscle and disease. *Gene*, **569**(1): 14–20.

Shen FX, Huang XB, He GX, et al. 2023. The emerging studies on mesenchymal progenitors in the long bone. *Cell & Bioscience*, **13**(1): 105.

Sheng JJ, Jin JP. 2016. *TNNI1, TNNI2* and *TNNI3*: evolution, regulation, and protein structure–function relationships. *Gene*, **576**(1): 385–394.

Sherman BT, Hao M, Qiu J, et al. 2022. DAVID: a web server for functional enrichment analysis and functional annotation of gene lists (2021 update). *Nucleic Acids Research*, **50**(W1): W216–W221.

Stewart TA, Liang C, Cotney JL, et al. 2019. Evidence against tetrapod-wide digit identities and for a limited frame shift in bird wings. *Nature Communications*, **10**(1): 3244.

Sutherland MJ, Wang S, Quinn ME, et al. 2013. Zic3 is required in the migrating primitive streak for node morphogenesis and left–right patterning. *Human Molecular Genetics*, **22**(10): 1913–1923.

Swank S, Sanger TJ, Stuart YE. 2021. (Non)Parallel developmental mechanisms in vertebrate appendage reduction and loss. *Ecology and Evolution*, **11**(22): 15484–15497.

Thiem CE, Stegmann JD, Hilger AC, et al. 2022. Re-sequencing of candidate genes FOXF1, HSPA6, HAAO, and KYNU in 522 individuals with VATER/VACTERL, VACTER/VACTERL-like association, and isolated anorectal malformation. *Birth Defects Research*, **114**(10): 478–486.

Tokita M, Kuratani S. 2001. Normal embryonic stages of the chinese softshelled turtle *Pelodiscus sinensis* (trionychidae). *Zoological Science*, **18**(5): 705–715.

Varga Z, Varga M. 2022. Gene expression changes during the evolution of the tetrapod limb. *Biologia Futura*, **73**(4): 411–426.

Vlashi R, Zhang XG, Wu MR, et al. 2023. Wnt signaling: Essential roles in osteoblast differentiation, bone metabolism and therapeutic implications for bone and skeletal disorders. *Genes & Diseases*, **10**(4): 1291–1317.

Wanek N, Muneoka K, Holler‐Dinsmore G, et al. 1989. A staging system

for mouse limb development. *Journal of Experimental Zoology*, **249**(1): 41–49.

Wang BL, Fallon JF, Beachy PA. 2000. Hedgehog-regulated processing of Gli3 produces an anterior/posterior repressor gradient in the developing vertebrate limb. *Cell*, **100**(4): 423–434.

Wang LJ, You XL, Ruan DF, et al. 2022. TET enzymes regulate skeletal development through increasing chromatin accessibility of RUNX2 target genes. *Nature Communications*, **13**(1): 4709.

White MP, Theodoris CV, Liu L, et al. 2015. NOTCH1 regulates matrix gla protein and calcification gene networks in human valve endothelium. *Journal of Molecular and Cellular Cardiology*, **84**: 13–23.

Woltering JM, Irisarri I, Ericsson R, et al. 2020. Sarcopterygian fin ontogeny elucidates the origin of hands with digits. *Science Advances*, **6**(34): eabc3510.

Yakushiji-Kaminatsui N, Lopez-Delisle L, Bolt CC, et al. 2018. Similarities and differences in the regulation of *HoxD* genes during chick and mouse limb development. *PLoS Biology*, **16**(11): e3000004.

Yang SH, Andrabi M, Biss R, et al. 2019. ZIC3 controls the transition from naive to primed pluripotency. *Cell Repports*, **27**(11): 3215–3227. e6.

Ye XP, Liu XW. 2022. Wnt16 signaling in bone homeostasis and osteoarthristis. *Frontiers in Endocrinology*, **13**: 1095711.

Zhang B, He P, Lawrence JEG, et al. 2024. A human embryonic limb cell atlas resolved in space and time. *Nature*, **635**(8039): 668–678.

Zhang HL, Guo B, Yang ZQ, et al. 2017. ATRA signaling regulates the expression of COL9A1 through BMP2-WNT4-RUNX1 pathway in antler chondrocytes. *Journal of Experimental Zoology Part B: Molecular and Developmental Evolution*, **328**(6): 575–586.

Zhao ZB, Wang L, Bartom E, et al. 2019. β-Catenin/Tcf7l2–dependent transcriptional regulation of GLUT1 gene expression by Zic family proteins in colon cancer. *Science Advances*, **5**(7): eaax0698.

Zhu JJ, Patel R, Trofka A, et al. 2022. Sonic hedgehog is not a limb morphogen but acts as a trigger to specify all digits in mice. *Developmental Cell*, **57**(17): 2048–2062. e4.

Zhu SP, Kuek V, Bennett S, et al. 2019. Protein Cytl1: its role in chondrogenesis, cartilage homeostasis, and disease. *Cellular and Molecular Life Sciences*, **76**(18): 3515–3523.